THE ASTRONOMICAL JOURNAL, 120:393–406, 2000 July

MORPHOLOGY AND ENERGETICS OF THE MOLECULAR GAS WITHIN A CORE AND A DIFFUSE REGION IN THE FILAMENTARY DARK CLOUD GF 9

DAVID R. CIARDI
Department of Astronomy, University of Florida, 211 Space Sciences Building, Gainesville, FL 32611; ciardi@astro.ufl.edu
CHARLES E. WOODWARD[1,2]
Department of Geology and Geophysics, University of Wyoming, Laramie, WY 82071-3905; chelsea@tana.irastro.uwyo.edu
DAN P. CLEMENS
Institute for Astrophysical Research, Boston University, 725 Commonwealth Avenue, Boston, MA 02215; clemens@protostar.bu.edu
DAVID E. HARKER
Space Science Division, NASA Ames Research Center, MS 245-3, Moffet Field, CA 94035-1000; harker@corvus.arc.nasa.gov
AND
RICHARD J. RUDY
Aerospace Corporation, M2/266, P.O. Box 92957, Los Angeles, CA 90009; richard.j.rudy@aero.org
Received 1999 January 22; accepted 2000 March 15

ABSTRACT

We have performed a CO, ^{13}CO, and CS survey of a dense core region (GF 9–Core) and a diffuse filamentary region (GF 9–Fila) within the dark cloud GF 9 (LDN 1082). Spectra in each line were obtained toward 120 positions within each region covering areas of $8' \times 10'$. GF 9–Core is associated with the Class 0 protostar IRAS PSC 20503+6006, while GF 9–Fila has no associated IRAS point sources. The median CO excitation temperature of the core region is 7.2 ± 0.5 K; for the filament region, the median temperature is 7.8 ± 0.5 K. The mass derived from the LTE isothermal analysis of ^{13}CO is 53 ± 8 and 40 ± 6 $M_\odot$ for GF 9–Core and GF 9–Fila, respectively. Using near-infrared extinction data to trace the H_2 column density, the isothermal LTE assumptions for ^{13}CO appear to break down at $A_V \gtrsim 3$ mag. The near-infrared extinction data are used to correct the derived ^{13}CO column densities, yielding mass estimates that are $\sim$20% larger than the LTE-derived masses. The average H_2 volume densities for GF 9–Core and GF 9–Fila are $\sim 5000 \pm 700$ and $\sim 1700 \pm 200$ cm^{-3}. Each region contains a 15 ± 3 $M_\odot$ centrally condensed CS core, which is approximately 3 times more dense than the ambient ^{13}CO regions. In GF 9–Core, the high-density gas core appears to be physically associated with the IRAS point source. Both high-density cores appear to be in virial equilibrium; however, the CS line widths in GF 9–Core are almost twice as large as those measured in GF 9–Fila. Because GF 9–Core is associated with the Class 0 protostar PSC 20503+6006, the CS line widths may be enhanced by outflow or infall motion. The additional nonturbulent line-broadening component caused by outflow/infall motion required to explain the line width implies a supersonic velocity of at least 0.3 km s^{-1} (Mach 1.5).

Key words: ISM: abundances — ISM: clouds — ISM: individual (LDN 1082, GF 9) — ISM: kinematics and dynamics — stars: formation

1. INTRODUCTION

Filamentary dark clouds (FDC) or globular filaments (GF) are small molecular clouds containing somewhat regularly spaced dense core regions connected by filamentary, lower density gas and dust (Schneider & Elmegreen 1979). Previous investigations of FDCs have focused on the star formation properties of individual dense core regions within the FDCs (Benson & Myers 1989; Yang et al. 1991; Wiesemeyer 1997). In many cases, these studies have been part of general surveys of low-mass star formation regions (Myers & Benson 1983; Myers, Linke, & Benson 1983; Beichman et al. 1986; Benson & Myers 1989; Terebey, Vogel, & Myers 1989; Wu, Zhou, & Evans 1992; Goodman et al. 1993) and have not represented investigations of an individual FDC. As a result, little is known about the general star formation properties of individual FDCs or how the star formation process within the core regions and the filamentary regions compare.

Many of the core regions within FDCs are suspected of being engaged in the process of forming low-mass stars (e.g., Beichman et al. 1986), while the filamentary regions appear quiescent. FDCs, therefore, are an ideal laboratory for *comparative studies* of potential low-mass star forming and non–star-forming regions within the same host cloud. By comparing the structural and energetic properties of the different environments within a FDC, the distinct evolutionary paths of the core regions and filamentary regions may be revealed.

A multiwavelength observational study was undertaken toward two regions within the FDC GF 9 (LDN 1082; Schneider & Elmegreen 1979) to understand how the star formation process within a core region of a FDC compares to that within a filamentary region. The identification and selection of the core and filamentary regions (GF 9–Core and GF 9–Fila) are described in Ciardi et al. (1998; hereafter Paper I).

GF 9–Core, listed as GF9 3C in the Schneider & Elmegreen (1979) catalog, is associated with the IRAS point

[1] NSF Presidential Faculty Fellow.
[2] Now at Department of Astronomy, University of Minnesota, 116 Church Street, SE, Minneapolis, MN 55455.

TABLE 1

CENTRAL COORDINATES OF REGIONS OBSERVED WITHIN GF 9

Region	α	δ
GF 9–Core.....	20 50 07	60 04 31
GF 9–Fila.....	20 48 02	60 00 27

NOTE.—Units of right ascension are hours, minutes, and seconds, and units of declination are degrees, arcminutes, and arcseconds (1950.0).

source PSC 20503+6006 and is suspected of being engaged in star formation (L 1082C; Myers, Linke, & Benson 1983; Beichman et al. 1986; Benson & Myers 1989; Bontemps et al. 1996; Saraceno et al. 1996). Clemens, Kraemer, & Ciardi (2000), using *IRAS* (12, 25, 60, 100 μm) and ISO (80, 103, 155, 184, and 202 μm) infrared photometry, have fitted the spectral energy distribution of PSC 20503+6006 and found the source to be an extremely young (Class 0) protostar. The diffuse filamentary region has no IRAS point sources associated with it.

In Paper I the total mass, as traced by the near-infrared dust extinction of background stars, contained within each region was about 24 $M_\odot$, but only GF 9–Core was found to possess a centrally condensed high-extinction core ($A_V \gtrsim 10$ mag). GF 9–Fila showed no sign of a central condensation, and its extinction distribution was consistent with that of a cylindrical dust distribution of uniform density. The near-infrared high-extinction core in GF 9–Core is associated with the IRAS point source, though no near-infrared counterpart to PSC 20503+6006 was detected (K limit $\sim$ 16 mag).

In this study radio isotopic imaging spectroscopy of GF 9–Core and GF 9–Fila was performed to address the following questions: What are the temperature and density distributions of the molecular gas within each region? What are the molecular gas masses within each region? Are the distributions and masses similar or different for the core and filamentary regions? What are the energetics of the molecular gas within each region? Are the core and filamentary regions gravitationally bound? Does either region show evidence for molecular gas outflow or infall, indicative of protostellar activity? How does the distribution of molecular gas correlate with the distribution of dust within each region?

In this paper we present the maps and analyses comprising our radio isotopic imaging spectroscopic study. A summary of the observations is given in § 2. In § 3, we present a detailed analysis of the morphological and energetic properties of the molecular gas within the two regions in the filamentary dark cloud GF 9. We find that the average masses and temperatures of the regions are similar, while the volume density of the molecular gas in GF 9–Core is twice that seen in GF 9–Fila. Each region contains a high-density gas core which is of equal mass, but again the average volume density of the core in GF 9–Core is twice

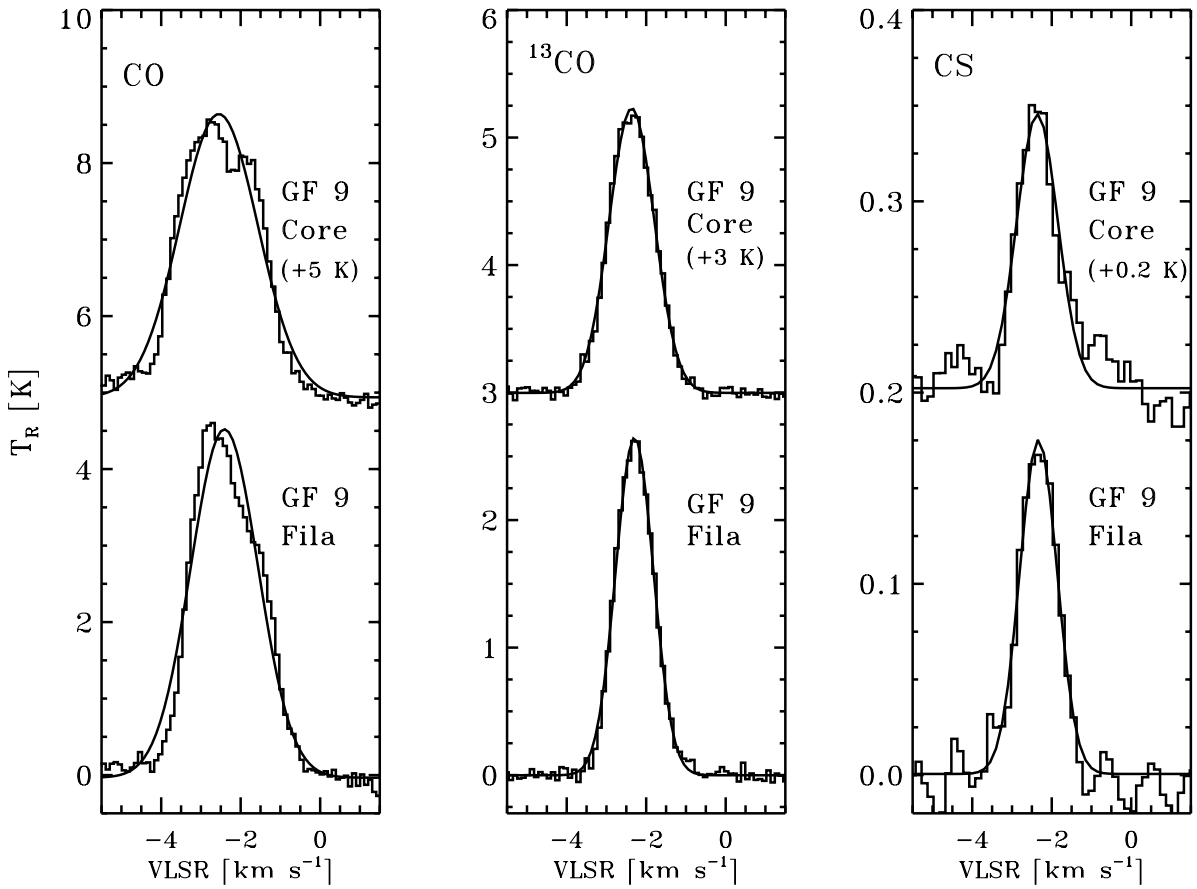

FIG. 1.—CO, ^{13}CO, and CS region–averaged spectra for both regions. The GF 9–Core spectra have been shifted vertically as indicated for clarity. The solid lines represent single Gaussian fits to the averaged spectra.

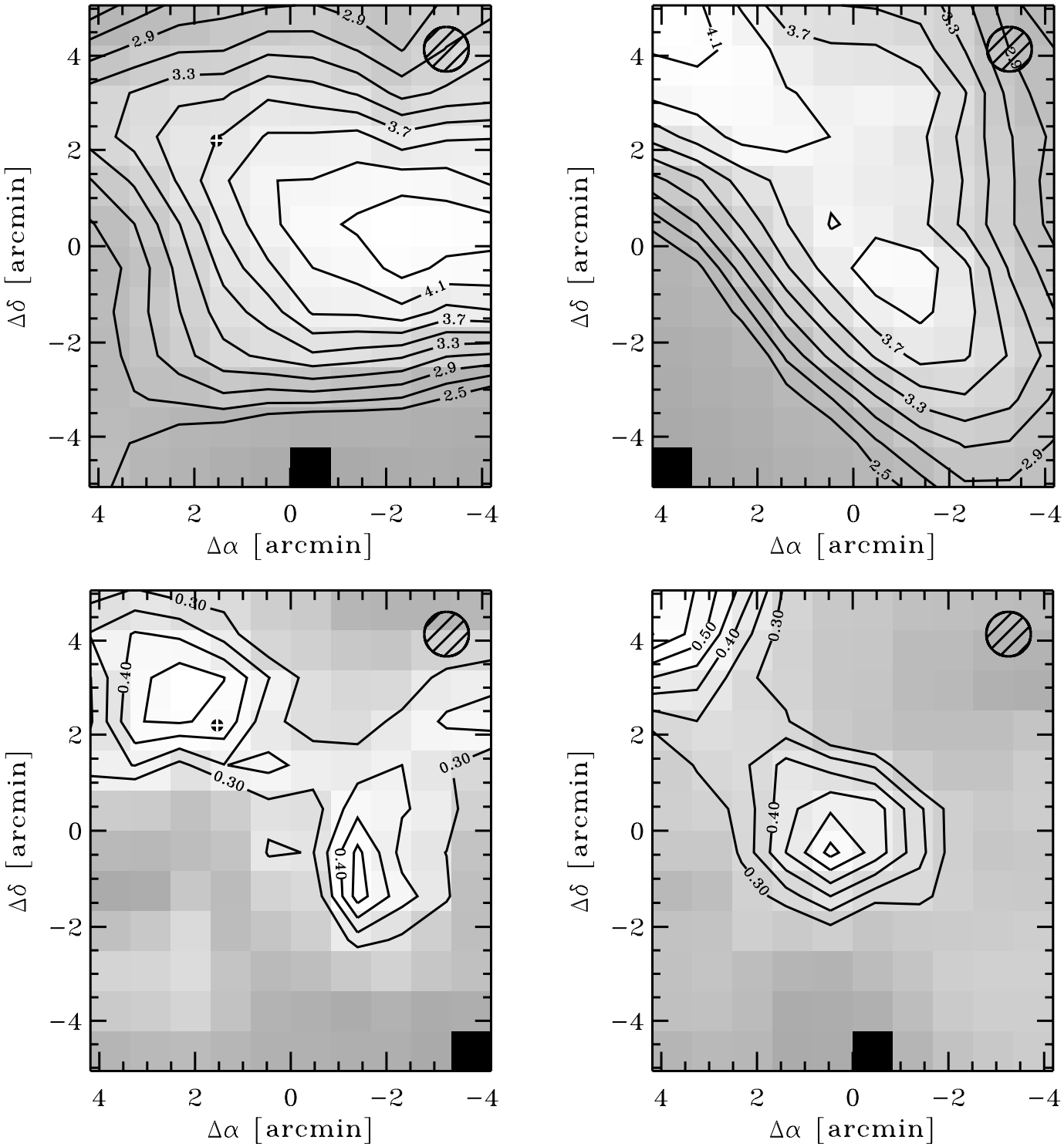

FIG. 2.—*Top*: ^{13}CO integrated intensity maps for GF 9–Core and GF 9–Fila. The contours start at 2.50 K km s^{-1} and are stepped in increments of 0.2 K km s^{-1}. The hatched circle in the upper right corner represents the approximate beam size of the observations (50″). The black circle with the white cross at ($\Delta\alpha = 1'.6, \Delta\delta = 2'.17$) in GF 9–Core marks the position of IRAS PSC 20503+6006. *Bottom*: CS integrated intensity maps for GF 9–Core and GF 9–Fila. The contours start at 0.30 K km s^{-1} and are stepped in increments of 0.05 K km s^{-1}. The hatched circle in the upper right corner represents the approximate beam size of the observations (50″). The black circle with the white cross at ($\Delta\alpha = 1'.6, \Delta\delta = 2'.17$) in GF 9–Core marks the position of IRAS PSC 20503+6006.

that of the core in GF 9–Fila. Both cores appear to be in virial equilibrium.

2. OBSERVATIONS AND DATA REDUCTION

Using the 14 m telescope of the Five College Radio Astronomy Observatory (FCRAO) in New Salem, MA, GF 9–Core and GF 9–Fila were observed spectroscopically in the rotational transitions of $^{12}C^{16}O$ ($J = 1 \rightarrow 0$; hereafter, CO), $^{13}C^{16}O$ ($J = 1 \rightarrow 0$; hereafter, ^{13}CO), and $^{12}C^{32}S$ ($J = 2 \rightarrow 1$; hereafter, CS) during the period 1995 December 11–13. Using the λ3 mm, 5 × 3 pixel QUARRY array, both regions were mapped twice in each rotational transition

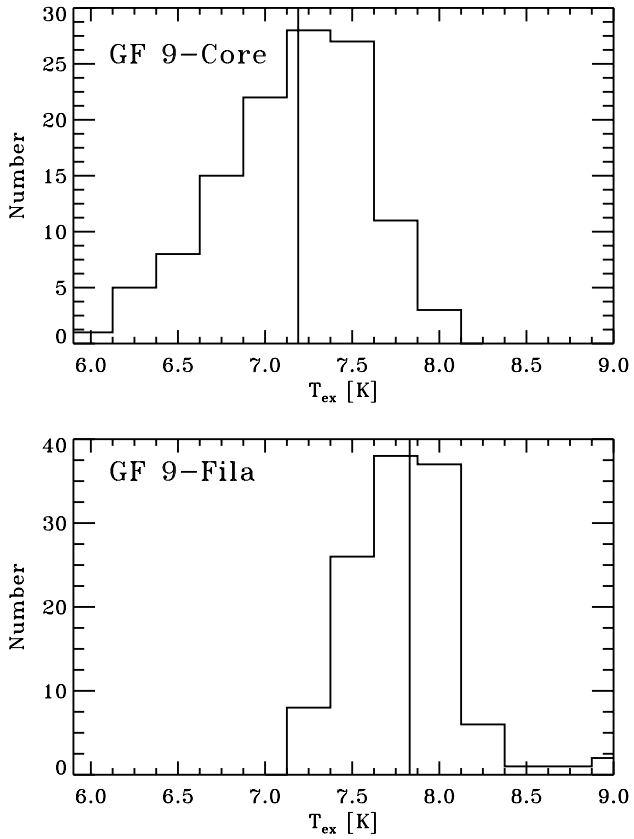

FIG. 3.—Histogram of the GF 9–Core (*top*) and GF 9–Fila (*bottom*) excitation temperatures calculated from the CO line profile peak intensity. The vertical lines represent the positions of the median temperatures, 7.2 and 7.8 K, respectively.

frequency at full beam width ($\sim 50''$) sampling, covering an area of approximately $8' \times 10'$. A total of 720 spectra were obtained toward GF 9, each with an integration time of 300 s; internal calibration was performed every 600 s. All observations were taken at elevation angles $>60°$. Central coordinates are listed in Table 1; optical images of the observed regions are shown in Paper I.

The focal-plane array autocorrelation spectrometer (FAAS) was utilized in the 1024-channel 10 MHz–wide configuration for all observations, yielding velocity resolutions of about 25 m s^{-1} channel^{-1}. The beam efficiencies ($\eta_B =$ 0.41, 0.46, 0.50 for CO, ^{13}CO, and CS, respectively) were adapted from the FCRAO Technical Report by Heyer[3] and applied to each of the reduced spectra. The average system temperatures were 700 K (CO), 550 K (^{13}CO), and 350 K (CS), respectively. Each CO and ^{13}CO spectrum was baseline-subtracted, folded and four-channel smoothed, except the CS spectra which were instead smoothed over six channels. Each position within the cloud was observed twice in each line. These spectra were averaged to produce final spectra with T_R rms noise levels of <0.8 (CO), <0.4 (^{13}CO), and <0.2 (CS) K channel^{-1}. Single Gaussian model profiles were fitted to each of the final spectra. The averaged spectra for each line toward the two regions are shown in Figure 1. The CO lines show some evidence for self-absorption, while the ^{13}CO and CS lines are well described by the single Gaussian fits. The integrated intensity maps of ^{13}CO and CS line emission are shown in Figures 2*a* and 2*b*.

[3] At http://donald.phast.umass.edu/~fcrao.

3. DISCUSSION

3.1. CO *and* ^{13}CO *Analysis*

3.1.1. *Excitation Temperature and Derived Column Densities*

The CO gas excitation temperature, under the assumptions of local thermodynamic equilibrium (LTE) and high CO optical depth, was computed for each line of sight through the cloud from the peak CO intensity via

$$T_R = \eta_c[J_\nu(T_{\rm ex}) - J_\nu(T_{\rm bg})](1 - e^{-\tau_\nu}) , \quad (1)$$

where η_c is the source coupling efficiency (assumed $\eta_c = 1$), τ_ν is the optical depth, $T_{\rm ex}$ is the excitation temperature, $T_{\rm bg}$ is the background radiation temperature, and J_ν is the source function

$$J_\nu = \frac{h\nu/k}{e^{h\nu/kT} - 1} . \quad (2)$$

In Figure 3 histograms of the derived CO excitation temperatures are shown for GF 9–Core and GF 9–Fila. The median temperatures for the two regions are 7.2 and 7.8 K, respectively. The standard deviations of the temperature distributions are approximately 0.5 K for each region. Myers, Linke, & Benson (1983) and Benson & Myers (1989), as part of a CO survey of nearby molecular clouds ($d \lesssim 900$ pc), measured an excitation temperature within GF 9–Core of 8 K for a $2'$ region centered on PSC 20503+6006, in reasonable agreement with the results found here.

LTE analysis of the ^{13}CO lines from GF 9 also assumed isothermal excitation with temperatures equal to the CO temperatures shown in Figure 3. Using equation (1), the ^{13}CO optical depth at each line of sight was computed, and the ^{13}CO column densities were estimated numerically as:

$$N(^{13}{\rm CO}) = \tau_\nu \frac{9.416(2\pi)^{1/2}}{A_{\rm ul}} \left(\frac{\nu}{c}\right)^3 \left(\frac{T_{\rm int}}{T_{\rm max}}\right) \times \left[\exp\left(\frac{h\nu}{kT_{\rm ex}}\right) - 1\right]^{-1} \exp\left(\frac{h\nu}{kT_{\rm ex}}\right) \frac{Z(T_{\rm ex})}{g_u} , \quad (3)$$

where τ_ν, ν, $A_{\rm ul}$, $T_{\rm int}$, $T_{\rm max}$, g_u, and $Z(T_{\rm ex})$ are, respectively, the optical depth, the frequency of the transition, the Einstein A coefficient, the measured line-integrated intensity, the measured line peak, the statistical weight of the transition, and the partition function (Genzel 1992). The resulting ^{13}CO column density maps for GF 9–Core and GF 9–Fila are shown in Figure 4.

In Figure 5*a*, the derived ^{13}CO column densities are compared with the near-infrared extinction along the same lines of sight. The extinction measurements were derived from the near-infrared database of Paper I. The mean near-infrared $(H-K)$ color excess was calculated for those sources that were within $50''$ of each line of sight in the radio maps. The weighted average line of sight extinction was computed from the mean color excess via $\langle A_V \rangle = \langle 15.9E(H-K) \rangle$. The reported extinction uncertainties are computed from the quadrature addition of the formal $E(H-K)$ measurement uncertainties and the standard deviation of $E(H-K)$ for those stars within a $50''$ bin. Details regarding the derivation of the extinction measurements can be found in Paper I. Note that the near-infrared data covered a

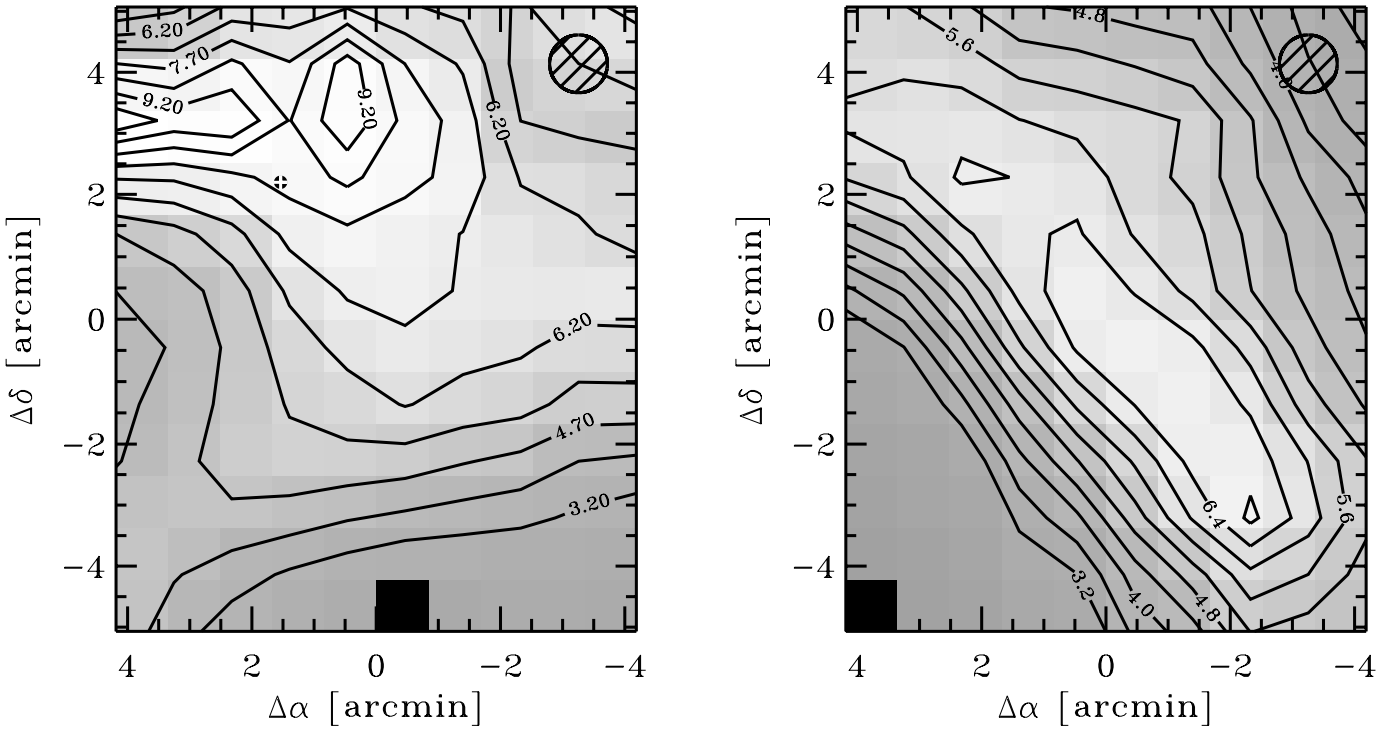

FIG. 4.—^{13}CO column density maps for GF 9–Core and GF 9–Fila. The contours start at 3.2×10^{15} cm^{-2} and are stepped by 0.75×10^{15} cm^{-2} and 0.4×10^{15} cm^{-2} for GF 9–Core and GF 9–Fila, respectively. The hatched circle in the upper right corner represents the approximate beam size of the observations (50″). The black circle with the white cross at ($\Delta\alpha = 1\farcm6, \Delta\delta = 2\farcm17$) in GF 9–Core marks the position of IRAS PSC 20503+6006.

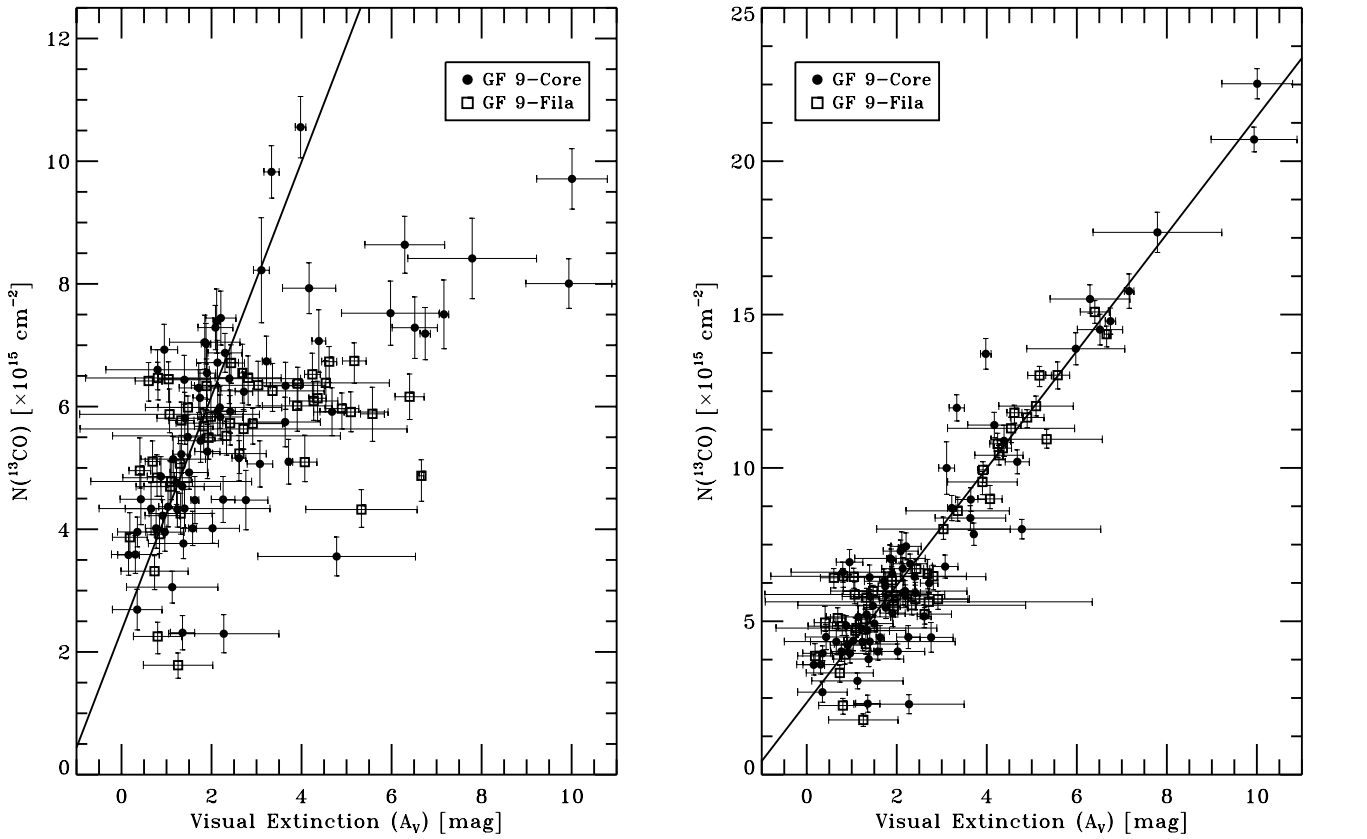

FIG. 5.—*Left*: Comparison of the ^{13}CO column densities with the near-infrared traced visual extinction. The line has been fitted to the data for $A_V \leq 3$ mag. *Right*: Comparison of the "A_V-corrected" ^{13}CO column densities with the near-infrared traced extinction (see § 3.1 for details). The best-fit line is the fit for the data at $A_V \leq 3$ mag shown in the panel on the left.

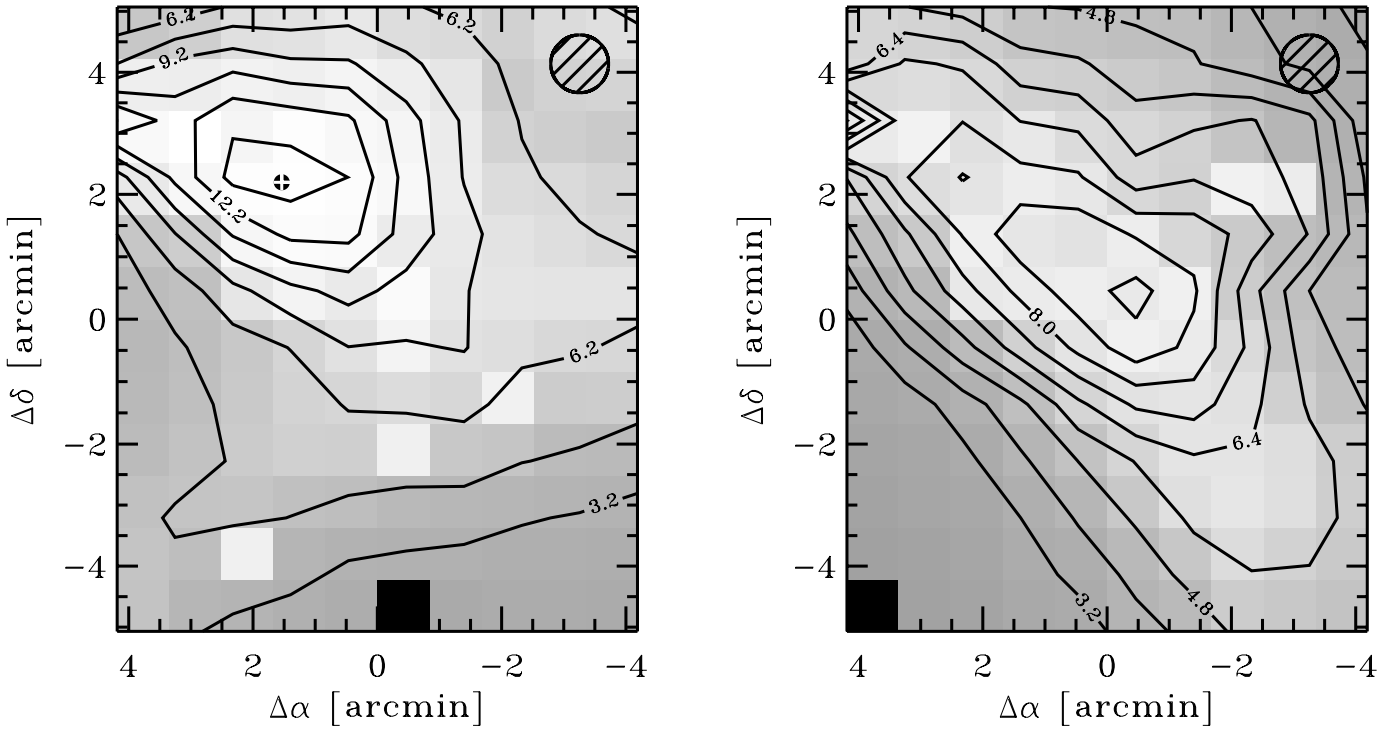

FIG. 6.—^{13}CO column density maps for GF 9–Core and GF 9–Fila after the ^{13}CO column densities have been "A_V-corrected" as described in the text. The images are a direct transformation of the maps shown in Fig. 4, while the contours were produced from a 2 pixel boxcar-smoothed image. The contours start at 3.2×10^{15} cm^{-2} and are stepped by 1.5×10^{15} cm^{-2} and 0.8×10^{15} cm^{-2} for GF 9–Core and GF 9–Fila, respectively. The hatched circle in the top right corner represents the approximate beam size of the observations (50″). The black circle with the white cross at ($\Delta\alpha = 1'.6, \Delta\delta = 2'.17$) in GF 9–Core marks the position IRAS PSC 20503+6006.

slightly smaller area on the sky; thus, only about 65% of the radio points have a corresponding extinction measurement.

Figure 5*a* shows a break in the ^{13}CO versus A_V relationship at $A_V \gtrsim 2$–3 mag. Using a two-dimensional least-squares fitting routine, which computes the resulting χ^2 using both the x and y uncertainties,[4] a linear fit was performed on the $A_V \leq 3$ mag points, with the following result:

$$N(^{13}\mathrm{CO}) = (2.4 \pm 0.2 \times 10^{15}\ \mathrm{cm}^{-2}) + \left(1.9 \pm 0.1 \times 10^{15}\ \frac{\mathrm{cm}^{-2}}{\mathrm{mag}}\right)(A_V)\ . \quad (4)$$

The data for the two regions (GF 9–Core and GF 9–Fila) were combined and fitted simultaneously, as the two regions do not appear to differ appreciably for $A_V \lesssim 3$ mag. Assuming a gas to dust ratio of 0.94×10^{21} H_2 molecules cm^{-2} mag^{-1} (Frerking, Langer, & Wilson 1982), the implied relative abundance of ^{13}CO to H_2 is $X(^{13}\mathrm{CO}) = N(^{13}\mathrm{CO})\ /N(\mathrm{H_2}) = (2.1 \pm 0.1) \times 10^{-6}$, in agreement with the standard ratio of Dickman (1978).

The data in Figure 5*a* located at $A_V > 3$ mag do not follow this trend. At $A_V > 3$ mag, the ^{13}CO to A_V relationship is shallower than for $A_V < 3$ mag. The flattening in the ^{13}CO to A_V ratio may result from the following. (1) A decrease in the gas-phase abundance of ^{13}CO at higher extinction could lower the measured ^{13}CO column density. However, depletion of the gas phase of CO is generally not observed until significantly higher densities ($n \sim 10^4$–10^5 cm^{-3}, Kramer et al. 1999; Caselli et al. 1999). (2) High-opacity regions (e.g., clumps), which are sampled by the high resolution of the near-infrared observations, but unresolved and beam diluted for the $\Theta_B \sim 50''$ ^{13}CO observations, could modify the relationship between the near-infrared extinction and ^{13}CO column density. Higher angular resolution observations of the gas are needed to address this issue. (3) A breakdown of the assumptions of isothermal LTE could lead to an overestimation of the excitation temperature in the central core and hence an underestimation of the ^{13}CO column density.

If we assume that the near-infrared extinction traces the true H_2 column density and that the true ^{13}CO column density to visual extinction ratio is constant throughout the cloud (i.e., a constant gas-to-dust ratio), then we can use the linear fit at lower extinction (eq. [4]) to derived correct ^{13}CO column densities. The ^{13}CO-A_V fit (eq. [4]) was subtracted from the data located at $A_V > 3$ mag, and the residuals were fitted with a line. This linear fit to the residuals was then added back to the originally derived ^{13}CO column densities (for $A_V > 3$ mag), effectively correcting each apparent ^{13}CO column density point to an ideal or true ^{13}CO value. The correction is, of course, a function of the measured extinction and ranges from 1–2 for $3 \lesssim A_V \lesssim 5$ to 2–3 for $A_V \gtrsim 5$. The resulting $N(^{13}\mathrm{CO})$ versus A_V relationship is shown in Figure 5*b*. The resulting column density maps are shown in Figure 6. The "A_V-corrected" maps retain the pixel-to-pixel variation inherent in the original extinction data.

The "noncorrected" ^{13}CO column densities (Fig. 5*a*) were derived based upon the assumption that the apparent CO excitation temperature applies to all of the ^{13}CO along each line of sight. However, because of the high optical

[4] Adapted from Press et al. (1992, p. 660).

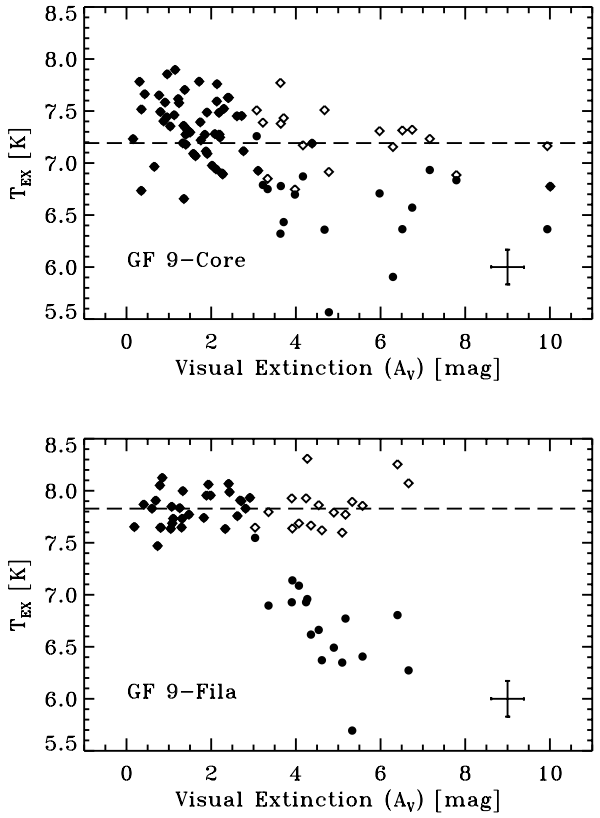

FIG. 7.—Comparison of the derived CO excitation temperatures with the near-infrared traced visual extinction for GF 9–Core (*top*) and GF 9–Fila (*bottom*). The open symbols are the temperatures derived directly from the CO line emission; the filled symbols are the temperatures derived from the "A_V-corrected" ^{13}CO column densities. The dashed lines represent the median temperatures marked in Fig. 3. Median uncertainties are shown in the bottom right of each plot.

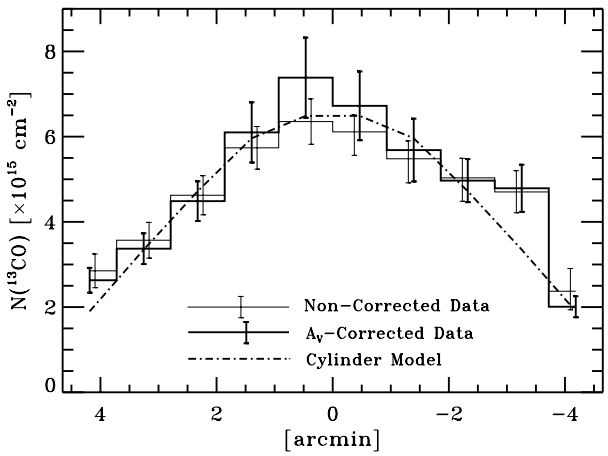

FIG. 8.—Comparison of average cross-axis cuts of the "noncorrected" and "A_V-corrected" ^{13}CO column density maps and the cylinder model. The cross-axis cuts were produced by averaging along the long axis of the cylinder, thereby, producing average cross-axis cuts across the filament axis.

depth, the CO line emission emanates primarily from lower density regions located in the outer (frontal) skin of the molecular cloud. If the central core of the cloud is colder than the outer skin, use of the apparent CO excitation temperature would overestimate the ^{13}CO excitation temperature existing deeper within the cloud. An overestimation of the ^{13}CO excitation temperature would lead, therefore, to an underestimation of the measured ^{13}CO column density.

If indeed the CO-derived excitation temperatures are too high for the ^{13}CO located at $A_V \gtrsim 3$ mag, then the "A_V-corrected" ^{13}CO column densities, coupled with the measured ^{13}CO line profiles, can be used to derive the *effective* CO excitation temperatures. For each point located at $A_V > 3$ mag, T_{ex} has been adjusted iteratively until the $N(^{13}CO)$ derived from equations (1)–(3) matches the column density (to within 10%) implied by the corresponding A_V (Fig. 5*b*). In Figure 7, the CO excitation temperatures derived directly from the CO line emission and the excitation temperatures implied by "A_V-corrected" ^{13}CO column densities are plotted as a function of visual extinction. Although the scatter is larger in GF 9–Core, the "A_V-corrected" effective excitation temperatures for both GF 9–Core and GF 9–Fila exhibit a decreased gas temperature for $A_V \gtrsim 3$ mag. This may indicate that the lower density (outer) portions of the cloud are warmer than the higher density (inner) portions of the cloud. The mean effective ^{13}CO excitation temperatures in the central cores of both GF 9–Core and GF 9–Fila are 6.5 ± 0.3 K.

3.1.2. *GF 9–Core*

Both versions of ^{13}CO column density maps (Figs. 4 and 6) contain a region of higher column density gas located near PSC 20503+6006. In Figure 4, the "noncorrected" column density peaks near $N(^{13}CO) = 10 \times 10^{15}$ cm^{-2}, and in Figure 6, the "A_V-corrected" column density peaks near $N(^{13}CO) = 22 \times 10^{15}$ cm^{-2}. The "A_V-corrected" map displays a more spherical ^{13}CO core than does the "noncorrected" map. However, this may be introduced by forcing the ^{13}CO and dust extinction to be linearly related (on average) throughout the cloud.

The ^{13}CO column densities were converted into H_2 column densities via the standard abundance ratio given by Dickman (1978): $X(^{13}CO) = N(^{13}CO)/N(H_2) = 2.0 \times 10^{-6}$. At a distance of 440 pc (Dobashi et al. 1994; Ciardi 1997; Ciardi et al. 1998) and with a 10% He mixture (Adler, Wood, & Goss 1996), the total ^{13}CO-traced mass contained within the $N(^{13}CO) = 5 \times 10^{15}$ cm^{-2} contour level is $53 \pm 8\ M_\odot$ ("noncorrected" column densities). For the same area, the "A_V-corrected" column density map yields a mass of $66 \pm 10\ M_\odot$.

The mass contained within the $N(^{13}CO) = 5 \times 10^{15}$ cm^{-2} contour [$N(^{13}CO) = 6 \times 10^{15}$ cm^{-2} for the "A_V-corrected" map] occupies an approximate projected area of $4' \times 2'$ at a position angle of $\sim 45°$. An assumption of prolateness ($4' \times 2' \times 2'$) yields an average ^{13}CO-derived, H_2 volume density of 5900 ± 700 cm^{-3} (7400 ± 800 cm^{-3} for the "A_V-corrected" column densities), while an assumption of oblateness ($4' \times 2' \times 4'$) yields a volume density of 2800 ± 300 cm^{-3} (3500 ± 400 cm^{-3} for the "A_V-corrected" column densities). The masses and densities are summarized in Table 2.

3.1.3. *GF 9–Fila*

The "noncorrected" and the "A_V-corrected" column density maps of GF 9–Fila look remarkably similar, both displaying a filamentary structure not seen in GF 9–Core. The "A_V-corrected" column density map displays a somewhat more centrally condensed region than does the "noncorrected" column density, but as with GF 9–Core,

TABLE 2

MASSES AND DENSITIES FOR GF 9 REGIONS

PARAMETER	GF 9–CORE		GF 9–FILA	
	Average[a]	CS Core[b]	Average[a]	CS Core[b]
Total mass [$M_\odot$]	53 ± 8	15 ± 3	40 ± 6	15 ± 3
	(66 ± 10)[c]	...	(48 ± 8)[c]	...
Projected radii (arcmin)	4×2	1.3	8×3	1.7
Projected size (pc)	0.51×0.26	0.16	1.02×0.39	0.22
$\langle n \rangle$ (cm^{-3})[d]	4400 ± 600	$15{,}000 \pm 3000$	1500 ± 200	6000 ± 1200
	(5500 ± 800)[c]	...	(1800 ± 300)[c]	...

[a] Parameters derived from ^{13}CO.
[b] Parameters derived from CS.
[c] Derived from "A_V-corrected" ^{13}CO column densities; see § 3.1.
[d] GF 9–Core mean ^{13}CO densities are averages of prolate and oblate estimates; for GF 9–Fila, cylindrical geometry was used; see § 3.1.2 for details.

this may be an artifact introduced by forcing the ^{13}CO and dust extinction to be linearly related throughout the cloud.

In Paper I, the distribution of dust (as traced by extinction) in GF 9–Fila was described by a two-component model comprised of a uniform density cylinder on top of a uniform background. A similar model was evaluated here to test whether the ^{13}CO gas distribution also can be described by a homogeneous cylinder plus uniform background. The model cylinder is infinitely long, viewed side-on, and of radius 3′. The peak line-of-sight column density of the cylinder was set to $N = 6.3 \times 10^{15}$ cm^{-2} and the background level was set to $N = 2.2 \times 10^{15}$ cm^{-2}. The total mass in the model was 63 $M_\odot$ and had an average H_2 volume density of 1,800 cm^{-3}. The model column densities correspond to visual extinction of $A_V = 3.4$ mag and $A_V = 1.2$ mag, in good agreement with the model values developed in Paper I. In Figure 8, an average slice across the long axis of the model is compared to average slices across the long axis of the "noncorrected" and "A_V-corrected" column density maps. The agreement between the model and the measured ^{13}CO distribution is good ($\chi^2/\nu \approx 1.5$), and the model works equally well for the

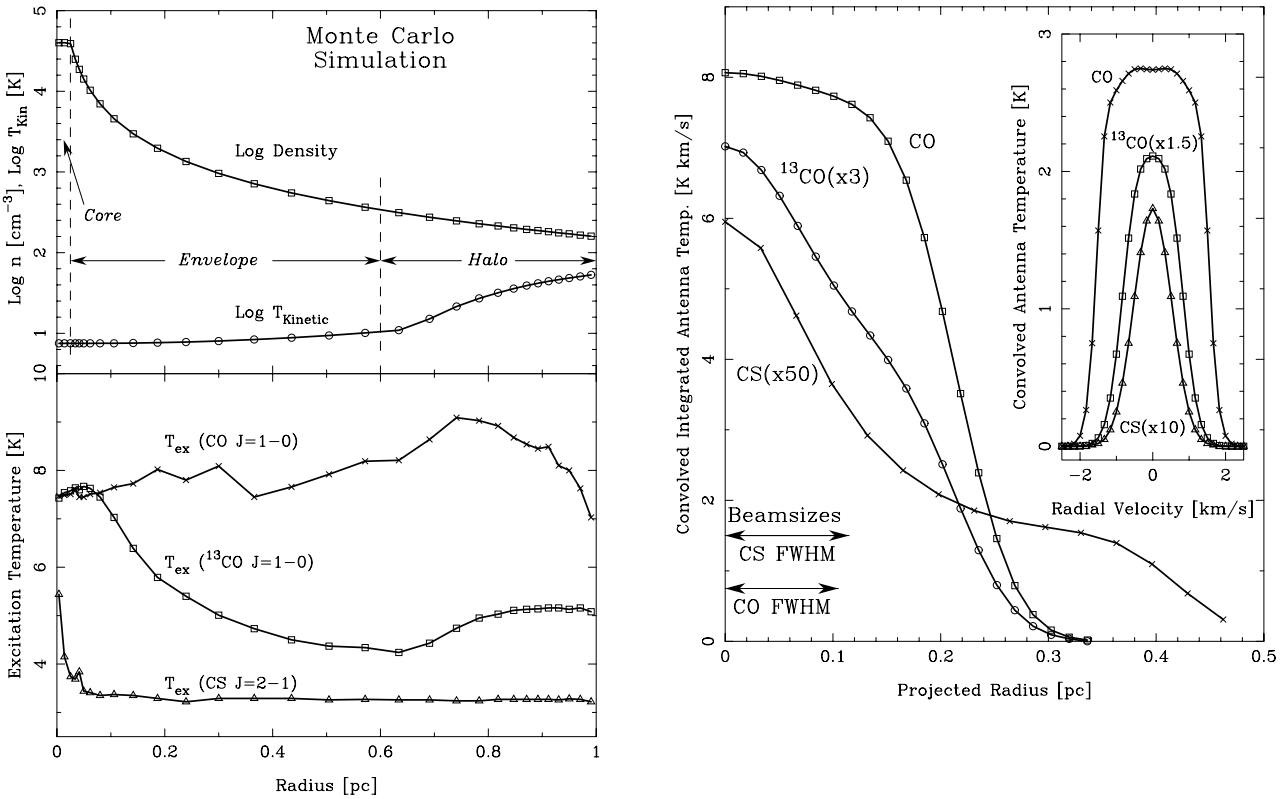

FIG. 9.—*Left*: Monte Carlo simulation inputs and outputs. *Top*: Input hydrogen density and temperature functions of radius. The density follows a $r^{-1.5}$ law outside the small core. The temperature function simulates the effects of external heating. The three model zones (core, envelope, and halo) are indicated. The points on each curve represent values calculated for each of the 30 model shells. *Bottom*: Calculated excitation temperatures for CO, ^{13}CO, and CS versus radius. *Right*: Monte Carlo simulated, beam-convolved profiles for the model cloud core. The curves follow the beam-convolved integrated antenna temperatures of the emergent lines versus projected offset. The ^{13}CO and CS profiles have been scaled up by 3 and 50. The convolving FWHM Gaussian beam sizes are shown in the lower left corner. *Inset*: Convolved line profiles for the central position (zero radius) show a progression in line strengths and widths. Here, the ^{13}CO and CS lines have been scaled up by factors of 1.5 and 10.

"noncorrected" and the "A_V-corrected" ^{13}CO column densities data. The model also reveals (highlights) that the southeast side of the column density distribution filament rises more steeply than the northwest side, possibly as a result of the cloud being influenced by a stellar wind or shock wave.

The mass contained within the $N(^{13}\mathrm{CO}) = 5 \times 10^{15}$ cm^{-2} contour is 40 ± 6 $M_\odot$ (48 ± 8 $M_\odot$ for the "A_V-corrected" map). Using a uniform cylinder similar to the model described above ($l = 8'$; $r = 3'$), a mean ^{13}CO-traced H_2 volume density of 1500 ± 200 cm^{-3} (1800 ± 300 cm^{-3}) is derived for the mass contained within these cylindrical boundaries. The mass and density of GF 9–Fila are summarized and compared to the values for GF 9–Core in Table 2.

3.2. CS *Analysis*

3.2.1. *Excitation Temperature and Derived Column Densities*

CS, with its large dipole moment (2 debye), requires relatively high densities ($n \gtrsim 10^4$ cm^{-3}) for thermalization at low (~ 10 K) temperatures (e.g., Genzel 1992). Possessing no additional isotopic or transitional information, we have estimated the excitation temperature of the CS from the results of Monte Carlo modeling (Bernes 1979) of the GF 9 regions.

The goal of the Monte Carlo modeling was to ascertain excitation temperatures for the CS $J = 2 \rightarrow 1$ line for cloud core conditions similar to those inferred for GF 9. We did *not* attempt to develop a complete model which explains all of the observed GF 9 core properties. Therefore, some input model parameters were fixed and some were adjusted until reasonable agreement was found between the observed and modeled central line profiles (heights, widths, shapes) and FWHM core sizes in the CO, ^{13}CO, and CS lines.

The spherically symmetric model contained three zones (a core, an envelope, and a halo), spanned by 30 concentric shells. The shell spacing varied and was finer at the cloud center and edge. The model was tuned until the central line profiles were in good agreement with the average CO, ^{13}CO, and CS profiles shown in Figure 1, and the FWHM sizes of the model core was in good agreement with the measured size listed in Table 2. The model cloud was also required to have a total mass and central A_V value near the values inferred from the ^{13}CO analysis.

A best match was found by simultaneously tuning the model core density, the core radius, the temperature function with radius, and the molecular abundances. The core radius and core density values mostly affect the inferred model cloud sizes and the line fluxes of ^{13}CO and CS. The temperature function mostly affects the CO line shape, especially the presence or absence of self-absorption, while abundances affect line widths and integrated line intensities.

The 1 pc model cloud core had a hydrogen molecule volume density which varied with radius outside the core zone as $r^{-1.5}$:

$$n(r) = \begin{Bmatrix} n_0 & r \le r_{\mathrm{core}} \\ n_0 (r/r_{\mathrm{core}})^{-1.5} & r > r_{\mathrm{core}} \end{Bmatrix}. \quad (5)$$

Values of $n_0 = 40{,}000$ H_2 cm^{-3} and $r_{\mathrm{core}} = 0.025$ pc (much smaller than our telescope beam) were found to produce model lines in good agreement with the observed lines. At the other zone outer boundaries the hydrogen densities were 340 cm^{-3} (envelope, to 0.06 pc) and 160 cm^{-3} (halo, to 1.0 pc).

To simulate external heating by the interstellar radiation field, the kinetic temperature in the model increased outward as:

$$T_{\mathrm{kin}} = \begin{Bmatrix} T_0 & r \le r_{\mathrm{core}} \\ T_0(1 + 0.5[(r - r_{\mathrm{core}})/(r_{\mathrm{env}} - r_{\mathrm{core}})]^{\beta_1}) & r_{\mathrm{core}} < r \le r_{\mathrm{env}} \\ T_0(1.5 + 6[(r - r_{\mathrm{env}})/(r_{\mathrm{halo}} - r_{\mathrm{env}})]^{\beta_2}) & r_{\mathrm{env}} < r \le r_{\mathrm{halo}} \end{Bmatrix}, \quad (6)$$

where $T_0 = 7.5$ K, $\beta_1 = 2$, and $\beta_2 = 1$. This produced a temperature profile which rises slowly with radius through the envelope (from 7.5 to 10.9 K) and increases more strongly through the halo (to 53 K). In Figure 9, the top panel shows the runs of model hydrogen density and temperature with radius.

The microturbulent line width was fixed at 0.7 km s^{-1} FWHM for all species and did not vary with radius. Similarly, abundances of CO, ^{13}CO, and CS relative to H_2 did not vary with radius. A constant background temperature of 2.74 K was included in the radiation field calculation and was subtracted from emergent line profiles to simulate observed lines. There were no velocity gradients in the model.

The program calculated emergent line profiles as a function of impact parameter. A set of two-dimensional convolutions of these line profiles with Gaussian telescope beam shapes were computed to simulate model line spectral profiles and profiles of line emission versus projected radius for comparison with the observations.

The simulated cloud which appeared to be a good match to our measured core properties had a total H_2 mass of 66 $M_\odot$. Although we followed its H_2 distribution out to 1 pc radius, the HWHM beam-convolved sizes were only 0.21 pc, 0.17 pc, and 0.13 pc for CO, ^{13}CO, and CS respectively. The abundances which produced reasonable line properties were 5×10^{-5}, 8.3×10^{-7}, and 4×10^{-10} for CO, ^{13}CO, and CS. For ^{13}CO and CS, these represent *lower* limits, since we compared model line profiles for the center map position to *average* observed cloud core profiles. The hot edge of the model cloud was successful in removing almost all of the self-absorption in the CO line which would normally be present in an isothermal microturbulent model.

The resulting runs of excitation temperature for the CO, ^{13}CO, and CS lines appear in the bottom panel of Figure 9. The high optical depth of the CO line keeps its T_{ex} high until the very edge of the cloud is reached. Such an almost flat T_{ex} is needed to avoid self-absorbed line profiles. The ^{13}CO T_{ex} falls quickly with radius, following a distribution similar to the $\log(n)$ curve in the panel above. The CS excitation temperature falls to about 3.5 K immediately outside the core region as the density becomes too low to populate easily this transition via collisions.

Figure 9 (*right panel*) shows the projected radial profiles of CO, ^{13}CO, and CS after convolving with two-dimensional Gaussians representing the FCRAO beams, with FWHM values of 48" and 54" (shown in the lower left corner of the figure). Although the radial profiles are different for the three species, the progression in FWHM sizes matches the observed progression well. Of interest to note is the long, faint CS tail to large projected radius. The central line profiles, convolved with the model telescope beams, are shown in the inset in the right panel of Figure 9.

Based upon the Monte Carlo modeling, the CS excitation temperature was fixed as $T_{\mathrm{ex}}(\mathrm{CS}) = \frac{1}{2}\langle T_{\mathrm{ex}}(\mathrm{CO})\rangle$ which,

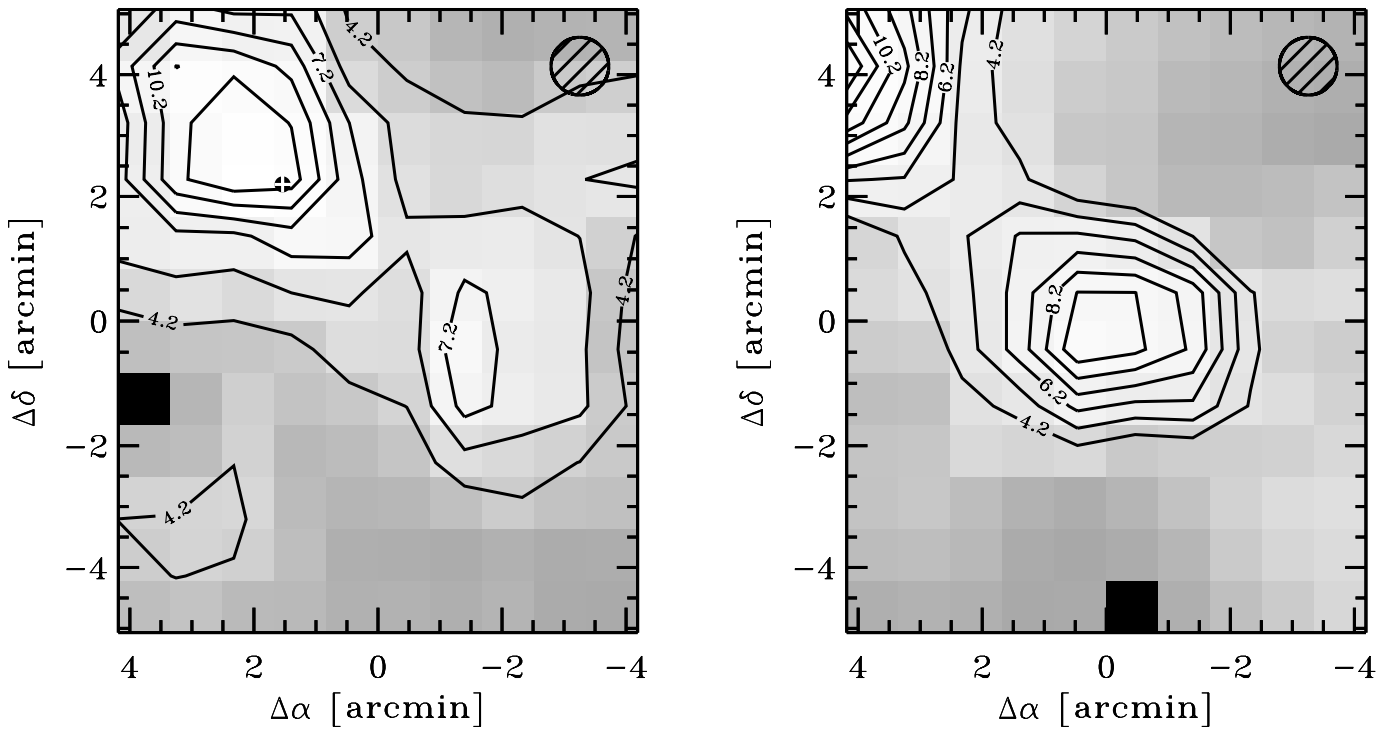

FIG. 10.—CS column density maps for GF 9–Core and GF 9–Fila. The contours start at 4.2×10^{12} cm^{-2} and are stepped by 1.5×10^{12} cm^{-2} and 1.0×10^{12} cm^{-2} for GF 9–Core and GF 9–Fila, respectively. The hatched circle in the top right corner represents the approximate beam size of the observations (50″). The black circle with the white cross at ($\Delta\alpha = 1'.6, \Delta\delta = 2'.17$) in GF 9–Core marks the position of IRAS PSC 20503+6006.

using equation (1), yielded optical depths $\langle\tau\rangle \approx 0.75$, $\tau_{\text{Core-peak}} \approx 5$, $\tau_{\text{Fila}-\text{peak}} \approx 3$. The CS integrated intensity maps were converted into column density maps via equation (3), and the resulting maps are shown in Figure 10.

In Figure 11, the derived CS column densities were also compared to the visual extinction derived from the database of extinction measurements of Paper I. CS and A_V are correlated over the full extent of the extinction range, with a Kendall-τ rank correlation probability of $>90\%$ (3 σ). The CS-A_V relationship shows no significant change at high A_V as did the ^{13}CO. A best-fit two-dimensional linear relationship of the form

$$N(\text{CS}) = (2.4 \pm 1.0 \times 10^{12}\ \text{cm}^{-2}) + \left(1.0 \pm 0.1 \times 10^{12}\ \frac{\text{cm}^{-2}}{\text{mag}}\right)(A_V) \qquad (7)$$

was derived; the slope of which implies a CS fractional abundance of $X(\text{CS}) = (1.1 \pm 0.3) \times 10^{-9}$. The highest CS signal-to-noise ratios ($\gtrsim 5$ σ) occur at the highest extinction ($A_V \gtrsim 2$–3 mag), where both the CS and near-infrared extinction measurements are most sensitive. Use of all of the data, however, leads to a y-intercept of the fit that is not well constrained. If we assume that the CS emission and the visual extinction must disappear together and force the y-intercept to be zero, the CS-A_V relationship has a steeper slope of $(1.4 \pm 0.2) \times 10^{12}$ cm^{-2} mag^{-1}, implying a CS fractional abundance relative to H_2 of $X(\text{CS}) = (1.5 \pm 0.2) \times 10^{-9}$. For L 134N, Swade (1989a) obtained an average fractional abundance for CS of $X(\text{CS}) = (7.0 \pm 1.6) \times 10^{-10}$.

In Figure 11, our two lines plus that for L 134N are shown for comparison. GF 9–Core and GF 9–Fila display no measurable differences in their CS abundances relative to H_2 within the scatter and uncertainties. The CS column densities were converted to H_2 column densities using the abundance ratio of $X(\text{CS}) = 1.5 \times 10^{-9}$. The masses are 50% lower than if the abundance ratio determined for L 134N (Swade 1989a) is used.

3.2.2. *GF 9–Core*

IRAS PSC 20503+6006 is located about 1′ southwest of a centrally condensed CS core. The CS column density is shown in Figure 12 as a function of radius from the center of the CS concentration: ($\Delta\alpha = 2'.1$, $\Delta\delta = 3'.0$). The core becomes indistinguishable from the background CS emission at a radius of $r \sim 2'$, with $\gtrsim 50\%$ of the mass contained within $r \sim 1'.3$ (0.16 pc). Applying the fractional abundance determined from Figure 11 to the CS column densities, the measured mass within $r = 1'.3$ is 15 ± 3 $M_\odot$. Assuming a spherical geometry, the average CS-associated H_2 volume density is $15{,}000 \pm 3000$ cm^{-3}, approximately 3–4 times the density of the ambient region. The core properties measured for GF 9–Core are summarized in Table 2.

The radial profile of the CS column density has been fitted with a power-law profile of the form $N(r) \propto r^{-0.72 \pm 0.10}$ (note that the data point at $r = 0'$ was not used in the fitting). The observed column density profile can be converted to a volume density profile via $\gamma = \alpha + 1 + \Delta\gamma$ where γ is the volume density power-law index, α is the column density power-law index, and $\Delta\gamma$ is a correction factor which takes into account the finite boundaries of the cloud. Yun & Clemens (1991) developed a method for determining $\Delta\gamma$ based upon the fractional radius of the cloud over which the core extends. The γ correction factor is estimated to be $\Delta\gamma = -0.2 \pm 0.1$ (Yun & Clemens

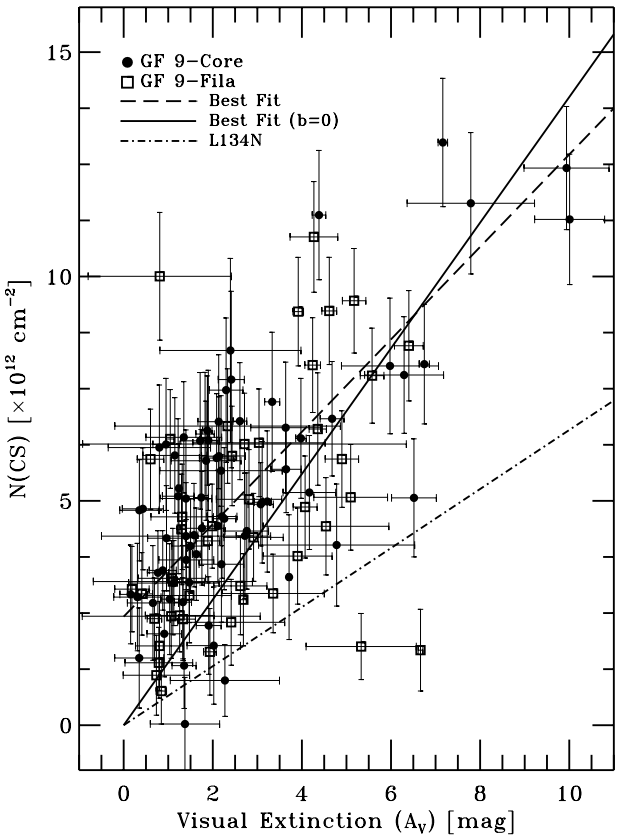

FIG. 11.—Comparison of the CS column densities with the near-infrared traced visual extinction. The dashed line represents the best-fit line for the relationship; the solid line represents the best-fit line after the y-intercept has been forced to equal zero; the dash-dot line represents the expected CS-A_V relationship for L 134N (Swade 1989a).

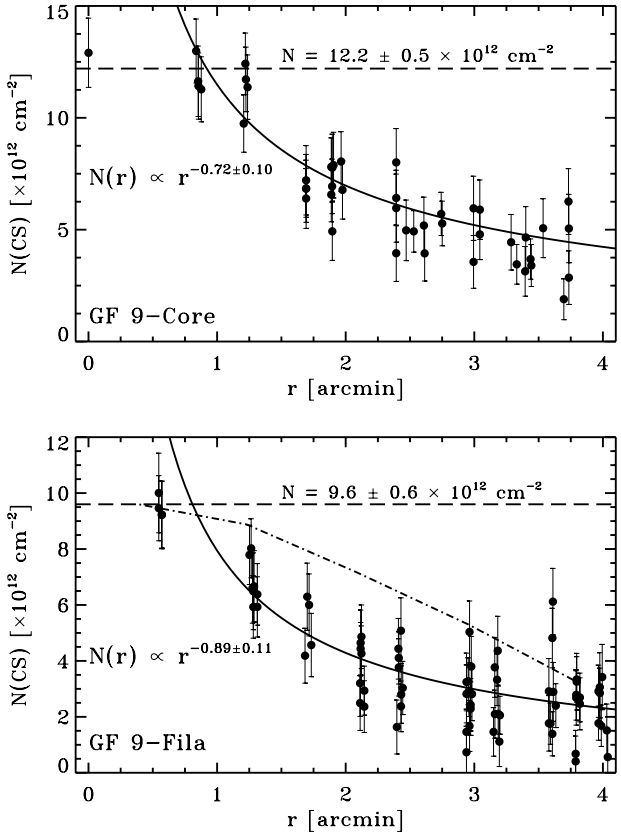

FIG. 12.—CS column density plotted against radial offset for GF 9–Core (*top*) and GF 9–Fila (*bottom*). The reference points for the offsets are ($\Delta\alpha = 2\farcm1$, $\Delta\delta = 3\farcm0$) and ($\Delta\alpha = 0\farcm0$, $\Delta\delta = 0\farcm0$) for GF 9–Core and GF 9–Fila, respectively. The solid line is the best-fit power law. The filled squares represent the map positions marked in Fig. 8. For GF 9–Fila (*bottom*), the radial profile expected from the cylinder model (Fig. 8) is plotted as the dash-dot line.

1991), yielding a volume density profile of the form $n(r) \propto r^{-1.5\pm0.2}$. This power-law density profile was assumed in the Monte Carlo modeling, as described earlier.

3.2.3. *GF 9–Fila*

As seen in the CS integrated intensity (Fig. 2*b*) and column density (Fig. 8) maps, GF 9–Fila contains a dense CS core, in contrast to the low density (^{13}CO-traced) gas distribution which appears mostly smooth and uniform. This phenomenon, of the lower density gas tracers (^{13}CO) not seeing the embedded high-density quiescent cores, is not unique to GF 9 (e.g., L 134N; Swade 1989b).

In Figure 12, the CS column density is plotted as a function of distance from the center of GF 9–Fila ($\Delta\alpha = 0'$, $\Delta\delta = 0'$). The CS core becomes indistinguishable from the background emission near a radius of $r \sim 2'$, with $\gtrsim 50\%$ of the mass contained within $r \sim 1\farcm7$ (0.22 pc). The mass traced by CS within this radius is $15 \pm 3\ M_\odot$. Assuming a spherical geometry, the CS core has a density of 6000 ± 1200 cm^{-3} which is approximately 2–3 times that of the ambient filament. The masses and densities for GF 9–Fila are summarized and compared to those of GF 9–Core in Table 2.

The CS core in GF 9–Fila is centrally condensed in a manner not revealed by the ^{13}CO column density. As discussed above, a uniform density homogeneous cylinder describes the ^{13}CO gas distribution fairly accurately. In Figure 12, the expected (cross-axis) radial profile of the cylinder model is plotted (*dash-dot line*) along with the radial distribution of the CS data. The CS data declines with radius more rapidly than would be predicted by the ^{13}CO distribution. The column density profile for the CS concentration in GF 9–Fila was fitted best with a power law of the form $N(r) \propto r^{-0.89\pm0.11}$. Again, the volume density γ correction factor is estimated to be $\Delta\gamma = -0.2 \pm 0.1$, yielding a volume density power-law profile of $n(r) \propto r^{-1.7\pm0.2}$.

The mass and temperature of the molecular gas within GF 9–Core and GF 9–Fila are quite similar, while the average ^{13}CO-traced H_2 volume density in the core region is about twice that in the filament region. Additionally, both regions contain CS-traced high-density gas cores which are of equal mass, but again the density of the core in GF 9–Core is twice that of the core in GF 9–Fila. How do these morphological properties relate to the energetic properties of the two regions? In the next section, we determine and compare the energetics of the two CS cores.

3.3. *Energetics and Gravitational Stability*

3.3.1. *Rotation*

The observed velocity gradients were determined by assuming that the velocity distribution of the CS spectra across the cores could be represented with solid-body rotation. Following the work of Heyer (1988), Clemens, Dickman, & Ciardi (1992), Kane (1995), and Kane & Clemens (1997), a matrix inversion method was used to

measure the mean positional velocity gradient across the CS cores in both GF 9–Core and GF 9–Fila. The planar fit returns both the velocity gradient and the direction of the associated angular momentum vector. The centroid velocities, determined from the single Gaussian fits, were used for the planar fitting and were weighted by the associated integrated intensity and velocity uncertainty. The method is inherently limited by the fact that all measured velocities are radial, and hence, the measured gradients are lower limits to the true velocity gradients. A mathematical description of the matrix inversion procedure is described in detail by Kane (1995) and Kane & Clemens (1997). The observed velocity gradients and derived angular momenta are given in the top of Table 3.

Both CS cores within GF 9 display very weak rotation. In agreement with our results, Goodman et al. (1993) also measured a weak NH_3 velocity gradient for a 2′ region surrounding IRAS PSC 20503+6006. Within their sample of dense cores Goodman et al. (1993) also found that the specific angular momentum (J/M) of the cores increases with core radius as $J/M = 10^{-0.7}R^{1.6}$ (km s^{-1} pc). Applying this relation to the CS cores in GF 9–Core ($R = 0.16$ pc) and GF 9–Fila ($R = 0.22$ pc), specific momenta of 10 m s^{-1} pc and 18 m s^{-1} pc, respectively, are predicted, in reasonable agreement with the measured values of 10 ± 2 m s^{-1} pc and 22 ± 6 m s^{-1}.

3.3.2. *Degree of Virialization*

The condition required for a core to collapse gravitationally is described by the scalar virial theorem $2T + U < 0$, where T is the sum of the kinetic energy terms and U is the sum of the potential energy terms. The support mechanisms (T) include rotational motion ($E_R = \frac{1}{5}MR^2(\omega/\sin i)^2$ where M is the core mass, R is the core radius, ω is the angular velocity, and i is angle of inclination), thermal motion ($E_T = \frac{3}{2}NkT$ where N is the total number of particles, and T is the kinetic temperature), and nonthermal motion [$E_N = \frac{3}{2}M(\Delta V^2/8\ln 2 - kT/m)$, where ΔV is the measured line width]. The binding energies (U) include self-gravitation ($E_G = \beta GM^2/R$ where β is related to the degree of central condensation[5]), and surface pressure ($E_S = 4\pi R^3 nkT$, where n is the average volume density of the medium surrounding the core Dickman & Clemens 1983; Arquilla & Goldsmith 1986).

Thus, if $2(E_R + E_T + E_N) < -(E_G + E_S)$, a molecular cloud core is gravitationally bound and may collapse if no other support mechanisms (e.g., magnetic fields) are present. For the CS cores contained within GF 9–Core and GF 9–Fila, the energy terms and their associated uncertainties have been estimated. The uncertainties were determined from the propagation of errors from the measurements; however, it should be noted that the potential energy terms are more strongly dependent upon the distance than the kinetic energy terms ($PE \propto d^3$; $KE \propto d^2$). Thus, an error in the (assumed) distance of 440 pc will affect not only the individual energy terms, but also the ratio of potential to kinetic energies. In addition, systematic uncertainties related to the CS excitation temperature and abundance may dominate the statistical uncertainties.

For each CS core, the energies were determined for the data contained within the radii listed in Table 2. The mean CS line widths (FWHM) are $\Delta V = 0.88$ km s^{-1} for GF 9–Core and $\Delta V = 0.57$ km s^{-1} for GF 9–Fila. The average line widths were corrected for the small degree of saturation (e.g., Dickman & Clemens 1983) using the mean CS optical depths ($\langle\tau\rangle = 0.75$). Table 3 summarizes the energetics for each of the observed CS cores: the observed velocity gradient (row [1]), angular momenta (row [2]), the specific momenta (row [3]), and the energies (rows [4]–[8]). The last column lists the Core-to-Fila energy ratios. The reported uncertainties represent only the estimated statistical uncertainties.

Both cores appear to be in virial equilibrium, with the gravitational and nonthermal energies contributing the largest fractions of the potential and kinetic energies, respectively. These are the only two types of energies where GF 9–Core shows larger values than GF 9–Fila. The slightly smaller size and higher mean density of the CS core in GF 9–Core causes the gravitational potential energy to be larger than the equal-mass CS core in GF 9–Fila. The difference in the nonthermal energies is a direct result of the average GF 9–Core CS line width being 50% broader than that measured in GF 9–Fila.

Interestingly, in an NH_3 survey by Goodman et al. (1993) of dense cores, an NH_3 line width of 0.53 km s^{-1} was measured for the region within 2′ of PSC 20503+6006, a value which is closer to the CS line width in GF 9–Fila, than to the CS line width in GF 9–Core. As NH_3 has a lower critical density ($\sim 10^4$ cm^{-3}) than CS ($\sim 10^5$ cm^{-3}), NH_3 is expected to be observed wherever CS is observed. However in many dense cores, the peaks of CS emission and NH_3 emission are found to be morphologically separated (Zhou et al. 1989). Zhou et al. suggest that the cores may

[5] $\beta = \frac{3}{5}$ for an homogeneous sphere and $\beta = 1$ for an infinite sphere with a volume density power-law profile of $n(r) \propto r^{-2}$. For the derived $n \propto r^{-1.5}$ volume density profiles, $\beta \approx 0.85$.

TABLE 3

ENERGETICS OF CS CORES

Parameter	GF 9–Core	GF 9–Fila	Core/Fila	Row
Observed ∇V (m s^{-1} arcmin^{-1}).....	120 ± 80	140 ± 70	0.9 ± 0.7	(1)
J (10^{12} $M_\odot$ km^2 s^{-1}).....	4.7 ± 1.0	10 ± 2	0.5 ± 0.2	(2)
J/M (m s^{-1} pc)	10 ± 2	22 ± 6	0.5 ± 0.2	(3)
E_R (10^{36} J)	0.14 ± 0.04	0.28 ± 0.07	0.5 ± 0.2	(4)
E_T (10^{36} J)	1.1 ± 0.3	1.2 ± 0.3	0.9 ± 0.3	(5)
E_N (10^{36} J)	4.5 ± 1.1	2.4 ± 0.6	2.0 ± 0.7	(6)
$\lvert E_S\rvert$ (10^{36} J)	0.9 ± 0.2	0.9 ± 0.2	1.0 ± 0.3	(7)
$\lvert E_G\rvert$ (10^{36} J)	10 ± 3.0	7.5 ± 1.9	1.3 ± 0.5	(8)
$R = (2T/U)$[a]	1.1 ± 0.3	0.9 ± 0.3	...	(9)

[a] Ratio of kinetic energy and potential energy terms.

become chemically differentiated as NH_3 becomes underabundant relative to CS in the presence of supersonic motion.

Typically, line widths are composed of two dominant constituents: thermal and turbulent motions. However, other gas motions (if present) such as outflow or infall, would broaden the lines. The line widths generally add together in quadrature (Myers, Ladd, & Fuller 1991) such that the observed line width may be represented as $\Delta V^2 = \Delta V_T^2 + \Delta V_\tau^2 + \Delta V_R^2 + \Delta V_X^2$, where ΔV is the observed line width, ΔV_T is the thermal component, ΔV_τ is the turbulent component, ΔV_R is the rotational broadening component, and ΔV_X is any additional (unresolved) motion component.

If the narrower NH_3 line width, observed toward GF 9–Core, is uncontaminated by significant bulk gas motion, the turbulent component of the CS velocity width may be estimated from the NH_3 nonthermal velocity width ($\Delta V_\tau \sim 0.52$ km s^{-1}). With $\Delta V_{CS} = 0.78$ km s^{-1} (after saturation correction), $\Delta V_T = 0.1$ km s^{-1}, $\Delta V_R = 0.20$ km s^{-1}, and $\Delta V_\tau = 0.52$ km s^{-1}, an additional line width component of size $\Delta V_X = 0.55$ km s^{-1} is calculated. This could originate with a small scale, but coherent, CS outflow/inflow with a velocity of at least $v \approx 0.3$ km s^{-1}.

The adiabatic sound speed for a cloud of temperature (T) and average particle mass (m) is given by $V_{ad} = (5kT/3m)^{1/2}$. For a gas kinetic temperature of 7 K and a mean molecular weight of $\sim$2.4 AMU, the sound speed is $\sim$0.2 km s^{-1}, indicating that the outflow/infall motion of the CS gas within GF 9–Core is marginally supersonic at a minimum of Mach (M_a) $\sim$ 1.5. The presence of supersonic motion may explain why the CS core in GF 9–Core is displaced from the NH_3 core. It must be cautioned that the outflow/infall velocity estimate is based upon the assumption that the NH_3 nonthermal line width is characterized *completely* by turbulent and thermal motions *and* that the CS turbulence is identical to the NH_3 turbulence.

Previous CO ($J = 2 \rightarrow 1$) studies by Wu, Zhou, & Evans (1992) and Bontemps, André, Terebey, & Cabrit (1996), concentrated at the position of the IRAS point source, which is spatially offset from the CS core, have found no evidence for an outflow in this region. However, profile fitting of the region-averaged CS spectra reveals a weak feature in the red wing of the best-fit Gaussian for only the GF 9–Core region (Fig. 1). This may be evidence for a weak outflow in GF 9–Core, though the low signal-to-noise of the wing feature in the individual spectra prevents spatial localization of the outflow. Clemens, Kraemer, & Ciardi (2000), via modeling of the infrared spectral energy distribution, have characterized the associated point source PSC 20503+6006 as a Class 0 protostar. Such a young source is expected to contain both outflow and infall bulk motions, as may be suggested by the broader CS line width in GF 9–Core. As most outflows associated with protostars and young stellar objects are more prominent in CO than in CS, we regard our evidence for an outflow associated with PSC 20503+6006 as weak but intriguing.

4. SUMMARY

The filamentary dark cloud GF 9 has been imaged spectroscopically in the rotational transitions of CO ($J = 1 \rightarrow 0$), ^{13}CO ($J = 1 \rightarrow 0$), and CS ($J = 2 \rightarrow 1$). The regions observed (GF 9–Core and GF 9–Fila) covered areas of $8' \times 10'$. The gas temperature, column density, mass, and density for each of the regions have been determined. In addition, the energy partitions of the CS cores within each region were determined and estimates of the degree of virialization were made. The following highlight the specific findings:

1. The average gas excitation temperature, derived directly from the peak intensity of the CO line emission, is 7.5 ± 0.5 K. GF 9–Core is colder than GF 9–Fila by $\sim$8%.

2. There is a break in the LTE-based $N(^{13}\mathrm{CO})$ versus A_V relationship at $A_V > 3$ mag, in the sense that the $N(^{13}\mathrm{CO})$ appears to be underestimated. The near-infrared extinction data have been used to correct the LTE-derived column densities to their "true" values; the correction factors are a function of the line of sight extinction and range from 1–3. The "A_V-corrected" column densities were inverted to derive *effective* excitation temperatures, which suggest that GF 9 may contain a warm (7.5 K) outer skin with a colder (6.0–6.5 K) interior.

3. The LTE-derived masses, as traced by ^{13}CO, of the core and filamentary regions are approximately 53 ± 8 and 40 ± 6 $M_\odot$, respectively. The "A_V-corrected" column densities yield mass estimates which are 20% larger. The mean density of the molecular gas in GF 9–Core is approximately 3 times that in GF 9–Fila.

4. Each region contains a centrally condensed CS core; both core masses are 15 ± 3 $M_\odot$. In both regions, the CS Cores are about 3 times more dense than the surrounding ambient cloud, as traced by ^{13}CO. The CS core in GF 9–Core is located approximately $1'$ to the northeast of the point source PSC 20503+6006, which has recently been identified as a Class 0 protostar (Clemens, Kraemer, & Ciardi 2000). Both CS cores are centrally condensed and are described by an average volume radial power-law index of $\gamma = -1.6 \pm 0.2$.

5. The CS cores appear to be in virial equilibrium. In both cores, gravitational potential and nonthermal motion are the dominant energies; however, the ratio of nonthermal energy to gravitational energy ($E_N/|E_G|$) in GF 9–Core is about 1.5 times that observed in GF 9–Fila. Because GF 9–Core is associated with the Class 0 protostar PSC 20503+6006, the CS line widths may be enhanced by supersonic outflow/infall motion. The additional nonturbulent line broadening component caused by outflow/infall motion required to explain the broader line width implies a supersonic velocity of at least 0.3 km s^{-1} (Mach 1.5).

In summary, both GF 9–Core and GF 9–Fila contain centrally condensed, high-density gas cores. The temperatures and masses of the two regions and of the cores contained within the regions are similar, but the densities in GF 9–Core are twice those of GF 9–Fila. Both high-density cores appear to be in virial equilibrium. However, the nonthermal kinetic energy properties of the two regions differ. The CS line widths in GF 9–Core are 50% broader than those in GF 9–Fila. The CS core in GF 9–Core may be experiencing supersonic outflow/infall motion, possibly indicative of ongoing protostellar activity. The radio observations of GF 9 have shown that the core and filamentary regions within FDCs are physically very similar but that the energetics may be different.

D. R. C. has been supported in part under NASA grant NGT-40050 and NASA WIRE ADP NAG 5-6751. D. R. C., C. E. W., and D. E. H. acknowledge support from the NSF under grant AST 94-53354 and the Office of Research, Uni-

versity of Wyoming. D. P. C. acknowledges support from NASA grant NAG 5-3337 and JPL 1207131. R. J. R. and the near-infrared camera have been supported in part by the Aerospace Sponsored Research Program. The authors would like to thank the referee, whose comments greatly improved the quality of this paper. D. R. C. would like to thank the staff at FCRAO for all their courteous support and help, both at the telescope and beyond. D. R. C. also thanks Elizabeth Lada for fruitful conversations regarding this work.

REFERENCES

Adler, D. S., Wood, D. O. S., & Goss, W. M. 1996, ApJ, 471, 871
Arquilla, R., & Goldsmith, P. F. 1986, ApJ, 303, 356
Beichman, C. Myers, P. C., Emerson, J. P., Harris, S., Mathieu, R., Benson, P. J., & Jennings, R. E., 1986, ApJ, 307, 337
Benson, P., & Myers, P. C. 1989, ApJS, 71, 89
Bernes, C. 1979, A&A, 73, 67
Bontemps, S., André, P., Terebey, S., & Cabrit, S. 1996, A&A, 311, 858
Caselli, P., Walmsley, C. M., Tapalla, M., Dore, L., & Myers, P. C. 1999, ApJ, 523, L165
Ciardi, D. R. 1997, Ph.D. thesis, Univ. Wyoming
Ciardi, D. R., Woodward, C. E., Clemens, D. P., Harker, D. E., & Rudy, R. J. 1998, AJ, 116, 349 (Paper I)
Clemens, D. P., Dickman, R. L., & Ciardi, D. R. 1992, AJ, 104, 2165
Clemens, D. P., Kraemer, K. E., & Ciardi, D. R. 2000, ApJ, submitted
Dickman, R. L. 1978, ApJS, 37, 407
Dickman, R. L., & Clemens, D. P. 1983, ApJ, 271, 143
Dobashi, K., Bernard, J., Yonekura, Y., & Fukui, Y. 1994, ApJS, 95, 419
Frerking, M. A., Langer, W. D., & Wilson, R. W. 1982, ApJ, 262, 590
Genzel, R. 1992, in The Galactic Interstellar Medium, ed., W. B. Burton, B. G. Elmegreen, & R. Genzel (New York: Springer), 275
Goodman, A. A., Benson, P. J., Fuller, G. A., & Myers, P. C. 1993, ApJ, 406, 528
Heyer, M. H. 1988, ApJ, 359, 363
Kane, B. D. 1995, Ph.D. thesis, Boston Univ.
Kane, B. D., & Clemens, D. P. 1997, AJ, 113, 1799
Kramer, C., Alves, J., Lada, C. J., Lada, E. A., Slevers, A, Ungerechts, H., & Walmsley, C. M. 1999, A&A, 342, 257
Myers, P. C., & Benson, P. J. 1983, ApJ, 266, 309
Myers, P. C., Linke, R. A., & Benson, P. J. 1983, ApJ, 264, 517
Myers, P. C., Ladd, E. F., & Fuller, G. A. 1991, ApJ, 372, L95
Press, W. H., Flannery, B. P., Teukolsky, S. A., & Vetterling, W. T. 1992, Numerical Recipes in C: The Art of Scientific Computing (Cambridge: Cambridge Univ. Press)
Saraceno, P., André, P., Ceccarelli, Griffin, M., & Molinari, S. 1996, A&A, 309, 827
Schneider, S., & Elmegreen, B. G. 1979, ApJS, 41, 87
Swade, D. A. 1989a, ApJ, 345, 828
———. 1989b, ApJS, 71, 219
Terebey, S., Vogel, S. N., & Myers, P. C. 1989, ApJ, 340, 472
Wiesemeyer, H. 1997, Ph.D. thesis, Rheinischen Friedrich-Wilhelms-Univ.
Wu, Y., Zhou, S., & Evans, N. J. 1992, ApJ, 394, 196
Yang, J., Umemoto, T., Takahiro, I., & Fukui, Y. 1991, ApJ, 373, 137
Yun, J. L., & Clemens, D. P. 1991, ApJ, 381, 474
Zhou, S., Wu, Y., Evans, N. J., III, Fuller, G. A., & Myers, P. C. 1989, ApJ, 346, 168